J. Fluid Mech. (2014), *vol.* 742, *pp* 152–170.
doi:10.1017/jfm.2013.659

Unsteady propulsion near a solid boundary

Daniel B. Quinn[1,†], Keith W. Moored[2], Peter A. Dewey[1] and Alexander J. Smits[1,3]

[1]Department of Mechanical and Aerospace Engineering, Princeton University, Princeton, NJ 08544, USA

[2]Mechanical Engineering and Mechanics, Lehigh University, Bethlehem, PA 18015, USA

[3]Monash University, Clayton Victoria 3800, Australia

(Received 12 July 2013; revised 3 October 2013; accepted 7 December 2013)

Experimental and computational results are presented on an aerofoil undergoing pitch oscillations in ground effect, that is, close to a solid boundary. The time-averaged thrust is found to increase monotonically as the mean position of the aerofoil approaches the boundary while the propulsive efficiency stays relatively constant, showing that ground effect can enhance thrust at little extra cost for a pitching aerofoil. Vortices shed into the wake form pairs rather than vortex streets, so that in the mean a momentum jet is formed that angles away from the boundary. The time-averaged lift production is found to have two distinct regimes. When the pitching aerofoil is between 0.4 and 1 chord lengths from the ground, the lift force pulls the aerofoil towards the ground. In contrast, for wall proximities between 0.25 and 0.4 chord lengths, the lift force pushes the aerofoil away from the ground. Between these two regimes there is a stable equilibrium point where the time-averaged lift is zero and thrust is enhanced by approximately 40 %.

Key words: flow-structure interactions, propulsion, swimming/flying

1. Introduction

Airfoils have long been known to achieve higher lift-to-drag ratios when operating near the ground, a phenomenon commonly called ‘ground effect’. In steady flight, ground effect has been extensively studied (see, for example, Coulliette & Plotkin 1996), and it has inspired the design of a number of aircraft (Rozhdestvensky 2006). Many animals are also known to use ground effect to improve their cost of transport and increase gliding distance, including herring gulls (Baudinette & Schmidt-Nielsen 1974), brown pelicans (Hainsworth 1988), black skimmers (Withers & Timko 1977), mandarin fish (Blake 1979), steelhead trout (Webb 1993), and flying fish (Park & Choi 2010). However, our understanding of ground effect is largely restricted to steady flow over fixed lifting surfaces, and the unsteady ground effects experienced by swimmers and flyers that oscillate their wings or fins have not been widely studied.

The first analytical approach to unsteady ground effect was taken by Tanida (2001), who applied the linearized Euler equations to a fluttering plate in a wind tunnel. There were two impermeable boundaries, one above and one below the plate, and

† Email address for correspondence: danielq@princeton.edu

this enforced symmetry does not represent the usual ground effect where only one wall is present. The study by Iosilevskii (2008) used asymptotics to predict the lift and drag on oscillating wings in weak ground effect, that is, where the ground proximity d is much greater than the chord length c, and the more interesting case where $d \leqslant c$ was not considered.

While several numerical studies of unsteady ground effect exist, only two have considered streamwise forces: Moryossef & Levy (2004) and Molina & Zheng (2011), who both examined an inverted Formula One car front wing undergoing heave oscillations. These studies focused on a velocity regime where the streamwise forces were mostly due to viscous drag, although the time-averaged drag was found to decrease near the ground and even switch to thrust at sufficiently high heaving frequencies.

Empirical evidence for unsteady ground effect is limited to a single recent study, that of Blevins & Lauder (2013), who measured the self-propelled swimming speed of a flexible fin modelled after a freshwater stingray. The fin underwent heave and pitch oscillations at the leading edge and was observed at two distances from the ground: $d \approx 0.2c$, and $d \approx c$. Over most conditions considered, no propulsive advantages were reported for near-ground swimming. However, some trends may have been due to flexibility, three-dimensionality, heave versus pitch considerations, or a combination thereof. The current study examines a simpler propulsor over a wider range of ground distances, the goal being to isolate the effect of ground proximity on unsteady propulsion.

An improved understanding of unsteady ground effect would help quantify the performance of swimmers and flyers in nature, and aid the design of unsteady propulsors, that is, thrust-producing devices that make use of unsteady hydrodynamics. Dual-foil propulsors, for example, consist of two aerofoils pitching in close proximity to each other, 180° out of phase, and Liu *et al.* (2010) have recently demonstrated that such propulsors show high levels of thrust and efficiency over a wide range of operation.

Motivated by such observations, we present new experiments and computations on the ground effect for a rigid aerofoil pitching near a planar boundary. We consider two main questions: to what extent do the advantages of steady ground effect apply to unsteady propulsors, and how is the wake behind such propulsors affected by the presence of the boundary?

2. Problem formulation

2.1. *Experimental methods*

Following Godoy-Diana *et al.* (2009), we use a foil with a semicircular leading edge that tapers along straight lines to its trailing edge (see figure 1). This shape was chosen for its symmetry and geometric simplicity. The foil was constructed of anodized aluminium with chord length $c = 79.35$ mm and span $s = 280$ mm. The maximum thickness of the foil, b, was set such that $b/c = 0.1$.

The foil is actuated so that its pitch angle follows $\theta = \theta_0 \sin(2\pi f t)$, where θ_0 is the maximum pitch angle, f is the oscillation frequency, and t is time. The ground proximity d is taken as the distance between the ground and the leading edge. The pitch oscillations dictate the peak-to-peak amplitude of flapping, $a = 2c \sin \theta_0$. We define the non-dimensional amplitude of oscillation $A^* \equiv a/c$, the non-dimensional ground distance $D^* \equiv d/c$, and the Strouhal number $St \equiv f a/u_\infty$, where u_∞ is the free-stream flow speed.

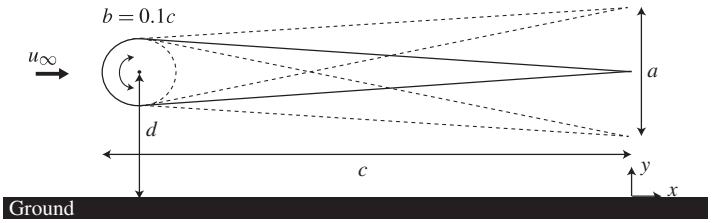

FIGURE 1. Length-scale definitions near the solid boundary. The relevant dimensions are chord length c, thickness b, pitching amplitude a, and ground proximity d. The origin is placed on the ground at the trailing edge, with y being the 'lateral' direction and x the 'streamwise' direction.

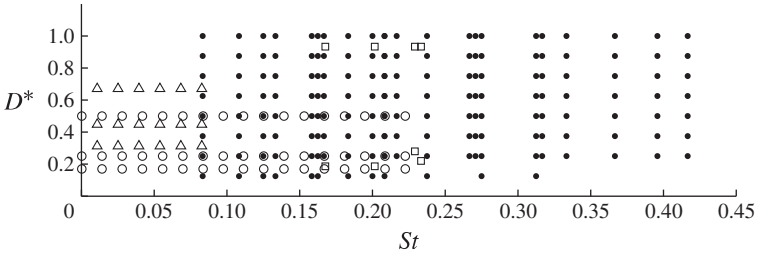

FIGURE 2. Parameters considered in the existing unsteady ground effect literature: Moryossef & Levy (2004) (△), Molina & Zheng (2011) (○), and Blevins & Lauder (2013) (□), as well as those considered in this study (●).

The foil was pitched about its leading edge using a servo motor (Hitec HS-7945TH), and its position was measured using an optical encoder (US Digital S1). In all experiments, the oscillation amplitude and the frequency varied from their input values by less than 0.5 % and 0.1 %, respectively. Data were taken at six flapping frequencies, equally spaced between 0.5 and 1.25 Hz, and three flapping amplitudes: 15, 20 and 25 mm ($A^* = 0.19$, 0.25 and 0.31, respectively). Each case was considered at eight ground proximities, seven ranging evenly from $D^* = 0.25$ to 1.01, and one at $D^* = 2.90$, which will be denoted $D^* \gg 1$. These D^* values were chosen to include those observed by Blevins & Lauder (2012), who quantified the kinematics of live freshwater stingrays swimming near a substrate. Figure 2 illustrates where the current study fits in with previous work in terms of Strouhal number and D^*, and we see that the present investigation is the first to consider high net thrust conditions where $0.25 < St < 0.45$.

The experiments were conducted in a closed-loop, free-surface water channel with a test section measuring 0.46 m wide, 0.29 m deep, and 0.244 m long. The foil spanned the entire depth of the water channel to minimize three-dimensional effects. The free-stream velocity was set to 0.06 m s^{-1}, giving a chord-based Reynolds number of $4700 \pm 3\%$, chosen to facilitate comparison with previous measurements in this facility and to be within the range experienced by the blue gill sunfish (see Drucker & Lauder 2001). The uncertainty reported is the standard deviation across the 2000 images used to calculate the free-stream velocity.

To measure the thrust produced, the actuation assembly was mounted on two air bushings (New Way Air Bearings S301901) which slid parallel to the free-stream flow direction (see figure 3). This arrangement allowed the assembly to press freely against a lever arm, which in turn pressed against a single point load cell (Omega

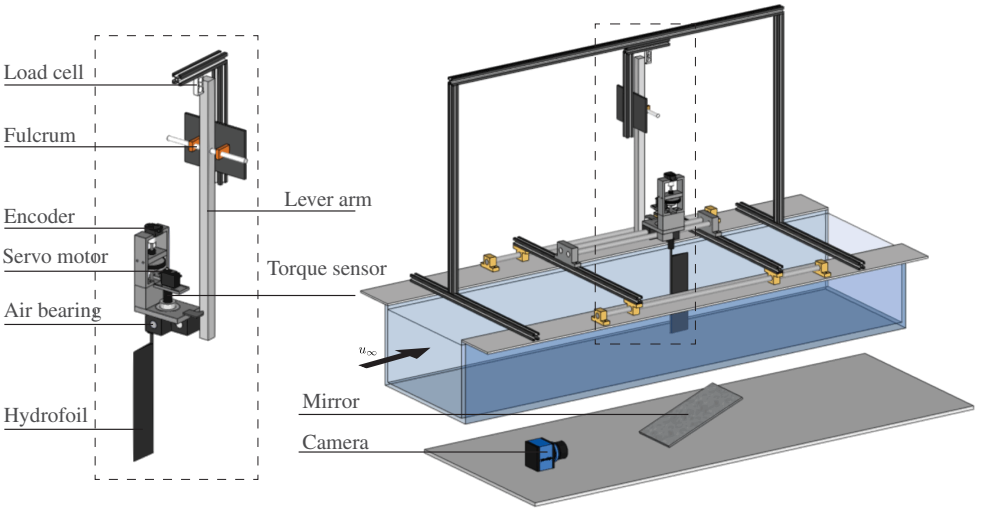

FIGURE 3. (Colour online) Experimental setup. The inset depicts the actuation mechanism.

LCAE-600). Further details are given by Buchholz & Smits (2008). The reaction torque ξ on the motor was measured using a torque sensor (Omega TQ-202) and the angular velocity $\dot{\theta}$ was found using the optical encoder. The power input to the system is then given by $f\int_{t_0}^{t_0+1/f}\xi\dot{\theta}\,\mathrm{d}t$, where t_0 is a reference time after which equilibrium swimming is assumed. For all cases considered, t_0 was set equal to 10 flapping cycles. To determine the power required to overcome the mechanical friction in the system, power data acquired with the foil removed were subtracted from all other power measurements. The average thrust $\bar{T}$ and power input to the fluid $\bar{P}$ were determined by integrating over 300 oscillation periods. The experimental variance was calculated for each condition by comparing 24 independent preliminary trials, and was found to be less than 7 % on $\bar{T}$, and 15 % on $\bar{P}$.

The force sensor measures the net streamwise force $\bar{F}_x$, equal to the thrust produced by the foil minus the drag imposed by the flow. We will use the term 'thrust' (T) in place of 'net force in the negative x direction' ($-F_x$), but in the strictest sense we always mean the latter. Similarly, the 'power' reported (P) is more precisely the 'power input to the fluid'.

To study the wake behaviour, particle image velocimetry (PIV) data were acquired for each case using a Nd:YAG laser (Litron Nano L 50-50) and a hybrid CCD/CMOS camera (LaVision, Imager sCMOS). The flow was seeded with neutrally buoyant hollow ceramic spheres with an average diameter of 10 μm. At the beginning of each oscillation period, a digital pulse was sent to a programmable timing unit (PTU) that triggered the laser and camera system. For phase-averaged data, the PTU discretized the oscillation period into eight phases which were averaged over 30 oscillation periods. For time-averaged data, 20 phases were used over 12 oscillation periods. Each data set therefore consisted of 240 image pairs. The velocity field was calculated using Davis 8.1.3, the spatial cross-correlation algorithm developed by LaVision Inc. (Stanislas *et al.* 2005). In total, four passes with 50 % overlap were conducted on the 2560 × 2160 pixel images: one with 128 × 128 pixel windows, one with 64 × 64, and two final passes with 32 × 32. The resulting velocity field consisted of 160 × 135 vectors. In quadrature, the average velocity

fields are estimated to have an uncertainty of 2.7 %, the instantaneous velocity errors are estimated to be 1 % to 5 % (Sciacchitano, Wieneke & Scarano 2013).

2.2. *Computational methods*

To model the flow over the foil, an unsteady two-dimensional potential flow method is employed where the flow is assumed to be irrotational, incompressible and inviscid. We follow Katz & Plotkin (2001), in that the general solution to the potential flow problem is reduced to finding a distribution of doublets and sources on the foil surface and in the wake that satisfy the no-flux boundary condition on the body at each time step. The elementary solutions of the doublet and source both implicitly satisfy the far-field boundary condition. We use the Dirichlet formulation to satisfy the no-flux condition on the foil body. To solve this problem numerically, the singularity distributions are discretized into constant-strength line boundary elements over the body and wake. Each boundary element is assigned one collocation point within the body where a constant-potential condition is applied to enforce no flux through the element. This results in a matrix representation of the boundary condition that can be solved for the body doublet strengths once a wake shedding model is applied. At each time step a wake boundary element is shed with a strength that is set by applying an explicit Kutta condition, where the vorticity at the trailing edge is set to zero so that flow leaves the aerofoil smoothly (Willis, Peraire & White 2007; Zhu 2007; Wie, Lee & Lee 2009; Pan *et al.* 2012).

At every time step the wake elements advect with the local velocity such that the wake does not support any forces. During this wake rollup, the ends of the wake doublet elements, which are point vortices, must be de-singularized for the numerical stability of the solution (Krasny 1986). At a cutoff radius of $\epsilon/c = 2.5 \times 10^{-5}$, the irrotational induced velocities from the point vortices are replaced with a rotational Rankine core model. The tangential perturbation velocity over the body is found by a local differentiation of the perturbation potential. The unsteady Bernoulli equation is then used to calculate the pressure acting on the body. The aerofoil pitches sinusoidally about its leading edge, and the initial condition is for the aerofoil trailing edge to move upward at $\theta = 0$.

The presence of the ground is modelled using the method of images, which automatically satisfies the no-flux boundary condition at $y = 0$ (see figure 4). At the smallest value of D^* considered (0.25), Strouhal numbers greater than 0.325 resulted in wake panels intersecting the foil boundary, and these conditions will not be reported here. Convergence studies found that the thrust and efficiency changed by less than 1 % and the power changed by less than 2 % when the number of body panels N ($= 250$) and the number of time steps per cycle N_t ($= 150$) were doubled. The computations were run for eight flapping cycles and the time-averaged data are obtained by averaging over the last cycle. After eight flapping cycles there was less than 1 % change in the thrust, power and efficiency when averaging over the seventh or eighth cycle. The numerical solution was validated using canonical steady and unsteady analytical results. The convergence and validation studies are described in more detail in appendix A.

2.3. *Viscous considerations*

A principal reason for comparing the experiments with the results of a potential flow solver is to help determine the conditions under which viscous effects become important. The potential flow method neglects all such effects, but in the experiment

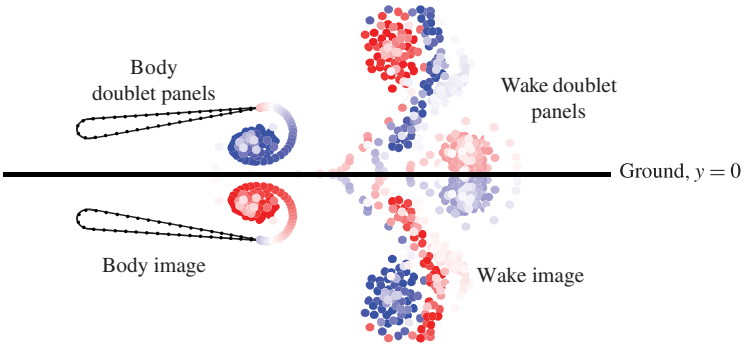

FIGURE 4. (Colour online) Illustration of the potential flow method. Circles designate the endpoints of doublet panels. The strengths of body panels are calculated at every time step, while the strengths of wake panels are known from previous iterations. All singularity elements are mirrored across the ground to satisfy the no-flux condition at $y = 0$. In the colour print, positive and negative vorticity in the wake are shown as red and blue, respectively.

there exist boundary layers on the foil, and at large pitch angles leading-edge separation may occur in the experiments (Kang *et al.* 2013). In addition, a boundary layer with thickness δ develops on the ground upstream of the foil, undoubtedly affecting the forces on the foil above a threshold value of δ/d. In the present study, a boundary layer thickness of 37 mm was measured using PIV, leading to $\delta/d \approx 2$ at the closest approach. A comparison between experiments and computations will help determine which ground effects are significantly affected by viscosity, and which are primarily inviscid phenomena.

3. Propulsive performance

Figure 5 shows the time-averaged thrust $\bar{C}_T$ and power $\bar{C}_P$ coefficients for $D^* = 0.63$ and $D^* \gg 1$, with $A^* = 0.25$, where

$$\bar{C}_T \equiv \frac{\bar{T}}{\frac{1}{2}\rho u_\infty^2 cs}, \quad \bar{C}_P \equiv \frac{\bar{P}}{\frac{1}{2}\rho u_\infty^3 cs}, \tag{3.1}$$

and ρ is the density of the fluid. As expected, the thrust and power are seen to increase monotonically with Strouhal number. More interestingly, both methods predict the thrust and power to rise monotonically as the foil approaches the ground. At $St = 0.38$, for example, the measured thrust coefficient, compared to its value at $D^* \gg 1$, shows an increase of 4 % at $D^* = 1$ ($\delta/d = 0.48$), 19 % at $D^* = 0.63$ ($\delta/d = 0.77$), 22 % at $D^* = 0.5$ ($\delta/d = 1$), and 44 % at $D^* = 0.38$ ($\delta/d = 1.3$).

The potential flow results show similar trends, although the absolute thrust is consistently overestimated by 20–30 % for $St > 0.3$ and up to 50 % for $St < 0.3$. The discrepancy is too large to be due to experimental variance alone, and presumably results from the computation excluding drag-producing effects such as skin friction drag, leading-edge separation, and interference with the ground boundary layer. This also leads to the relative gains in thrust being underestimated. As a comparison, the predicted increases at $St = 0.38$ were 4 % at $D^* = 1$, 10 % at $D^* = 0.63$, 16 % at

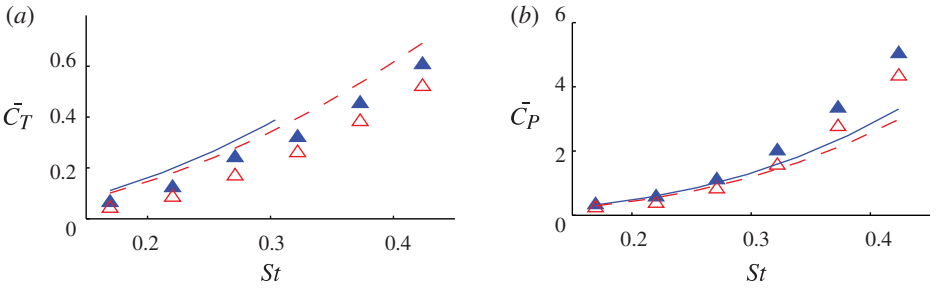

FIGURE 5. (Colour online) Time-averaged coefficients of thrust and power. $A^* = 0.25$. Experiment: △, $D^* \gg 1$; ▲, $D^* = 0.63$. Boundary element method: - - - - - -, $D^* \gg 1$; ———, $D^* = 0.63$.

$D^* = 0.5$, and 30 % at $D^* = 0.38$. The agreement between experiment and computation is better for the power data at low Strouhal numbers, although at higher Strouhal numbers the computation progressively underestimates the power input to the fluid, suggesting that viscous effects play an increasingly important role in scaling the moments on the foil.

Thus far the thrust and power coefficients were non-dimensionalized using the dynamic pressure. For unsteady flows, it may be more insightful to seek a scaling that expresses the unsteady characteristics of the flow. Theodorsen's (1935) model for a small-amplitude oscillating plate gives St^2 as the leading coefficient of both $\bar{C}_T$ and $\bar{C}_P$ (see appendix B for details). The model requires that $A^* \ll 1$, because $O(1)$ values lead to separated boundary layers along the foil and nonlinearly deforming wakes that affect the downwash. At higher values of A^*, we could expect a transition to a state where the lifting force on the foil L' scales with the unsteady dynamic pressure induced by the foil, that is, $L' \sim \rho(c\dot{\theta})^2 cs$, where $c\dot{\theta}$ is used as a typical lateral velocity. This new regime may have little effect on the streamwise component of lift (the thrust) because $L'\theta$ will integrate to zero over a flapping cycle due to the orthogonality of θ and $\dot{\theta}^2$ for sinusoidal motions.

The power, however, would scale differently. The moment on the foil scales with $L'c$ and so the power input scales with $L'c\dot{\theta}$, leading to

$$\bar{P} \sim \int_0^{1/f} L'c\dot{\theta}\,\mathrm{d}t \sim \rho s c^4 \int_0^{1/f} \dot{\theta}^3\,\mathrm{d}t. \tag{3.2}$$

By introducing $\Theta \equiv \theta/A^*$ and $\tau = f\,t$, this can be written in non-dimensional form as

$$\bar{C}_P \sim St^3 \int_0^1 \dot{\Theta}^3\,\mathrm{d}\tau. \tag{3.3}$$

To account for this possible transition from a St^2 to a St^3 scaling in the power, we propose a scaling of the form $St^{2+\alpha}$, such that $\alpha = 0$ corresponds to the $A^* \ll 1$ scaling and $\alpha = 1$ corresponds to the $A^* = O(1)$ scaling. We will verify this proposed scaling by experiment.

We now turn to the ground proximity D^*. If we take as a starting point the observation that the potential flow method is reasonably successful in representing the flow, combined with the fact that the potential flow equations are linear, a simple power law may apply to at least the leading-order terms of the time-averaged forces.

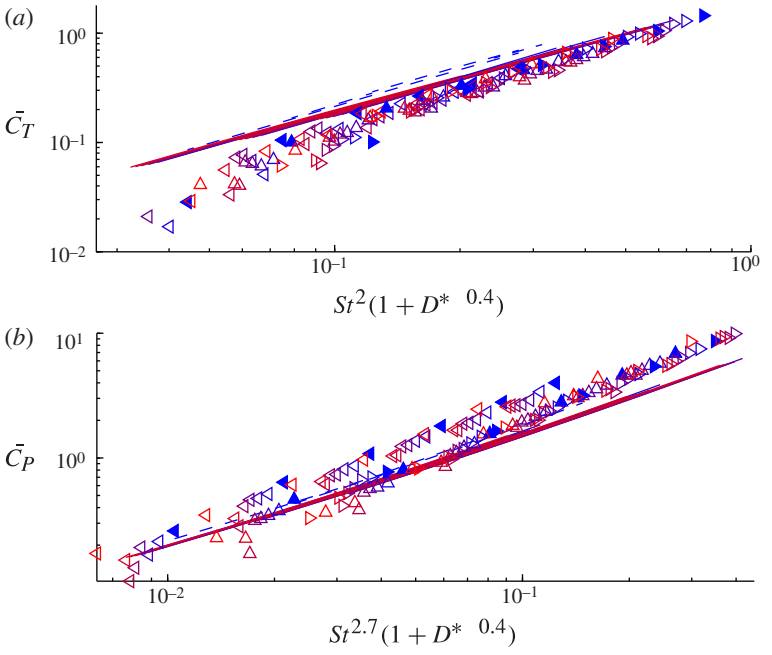

FIGURE 6. (Colour online) Thrust and power scaling. Experiment: ◁, $A^* = 0.19$; △, $A^* = 0.25$; ▷, $A^* = 0.31$. Boundary element method: - - - - - -, $D^* = 0.25$; ———, all other D^*. In the colour print, red corresponds to $D^* \gg 1$ and blue corresponds to $D^* = 0.25$, with intermediate values shaded accordingly. Filled symbols denote $D^* = 0.25$.

For the scaling to vanish far from the ground, we use $1 + D^{*-\beta}$, such that the final form of the proposed scaling is

$$\bar{C}_T \sim St^2(1 + D^{*-\beta}) \quad \text{and} \quad \bar{C}_P \sim St^{2+\alpha}(1 + D^{*-\beta}). \tag{3.4}$$

Figure 6 plots all the data in this form, where the values $\alpha = 0.7$ and $\beta = 0.4$ were determined empirically by minimizing the squared residuals. Overall, the collapse is excellent for both the experiment and computations, particularly at higher Strouhal numbers. However, the experiments and computations fall along curves with somewhat different slopes, where the computations overpredict thrust at low Strouhal numbers and underpredict power at high Strouhal numbers, as seen in the conventionally scaled results given in figure 5.

The propulsive efficiency η ($\equiv \bar{C}_T/\bar{C}_P$) represents the fraction of the total wake energy that results in streamwise kinetic energy gains for the propulsor. It is only defined in positive-net-thrust conditions when a propulsor is either accelerating or overcoming the drag on a body to which it is attached. The scaling given in (3.4) suggests that $\eta \sim St^{-\alpha}$ and that it should not depend on the distance from the ground.

Figure 7 indicates that at Strouhal numbers greater than ∼0.25, the experimental and predicted efficiency follows the trends which we expect from the scaling, that is, it decreases with St and is independent of D^*. At lower Strouhal numbers, however, circulatory forces and viscous effects cause the experimental efficiency to decrease, or even become negative. In this low-thrust regime, no dependence on D^* is observed, although the scatter in η prevents making a more definitive conclusion. The potential

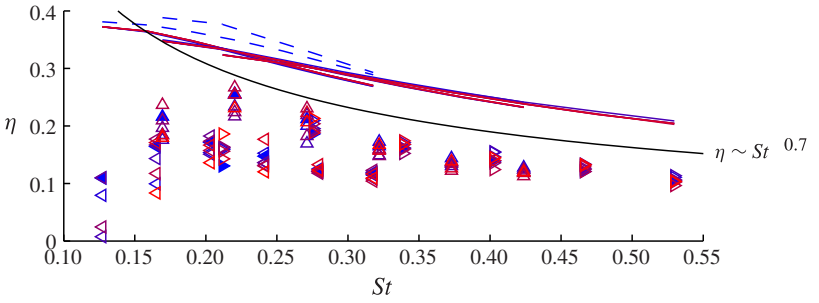

FIGURE 7. (Colour online) Propulsive efficiency. Symbols as in figure 6. The line $\eta = 0.1St^{-0.7}$ is also shown.

flow solver predicts η to be independent of D^*, except for the special case of $D^* = 0.25$, where efficiency is predicted to increase slightly for $St < 0.3$.

Despite the differences mentioned above, the bulk of the experiments and computations display similar qualitative trends. For all Strouhal numbers considered, they both show a monotonic increase in thrust with decreasing wall proximity. For $St \gtrsim 0.25$, this increase follows the same power law for both data sets, which suggests that the experiments show no strong dependence on δ/d in the regime considered (with $D^* = 0.25$ being a possible exception). Both data sets also indicate that the efficiency is unchanged by ground proximity at high Strouhal numbers. This observation has important consequences for near-ground swimming, in that by operating near the ground a propulsor could cruise faster with little loss in efficiency, or cruise at the same speed with increased efficiency. In general, it appears that the benefits of ground effect can be explained with an inviscid argument, although the magnitudes of the relative benefits clearly depend on viscous interactions.

4. Wake dynamics

The wake dynamics appear to be dominated by the vortices shed from the trailing edge. Leading-edge separation was observed in the experiments for $St > 0.2$, but vortices shed from the leading edge were significantly weaker than vortices shed from the trailing edge. As the foil approached the ground, leading-edge vortices were accentuated on the side closer to the wall, but they quickly became incoherent as they interacted with the ground boundary layer.

Vortices shed from the trailing edge were coherent and formed a typical vortex street when the foil was operated far from the ground (see figure 8*a*). In the figure, we define φ as the phase of the oscillation such that φ ranges from 0 to 2π and $\varphi = 0$ corresponds to the point in the cycle when $\theta = 0$ and $\dot{\theta} > 0$. A variety of symmetric vortex streets have been observed behind flapping propulsors (see, for example, Schnipper, Andersen & Bohr 2009), as well as some asymmetric ones (Godoy-Diana *et al.* 2009). For the parameters considered here, only a 2S reverse von Kármán street was observed far from the wall. Near the ground, however, this symmetry was broken and the vortices instead formed pairs (see figure 8*b*). This pairing was observed to some degree for all Strouhal numbers when $D^* < 1$, though was most prominent at high Strouhal numbers and low values of D^*. A similar pairing was noted by Molina & Zheng (2011), but they attributed it to asymmetries introduced by the camber of the foil. Here we have a symmetric foil, so that the vortex pairs appear to be a general feature of near-ground wakes.

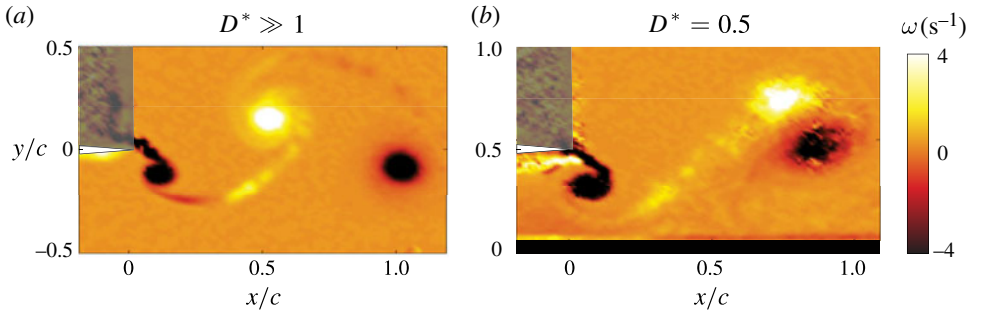

FIGURE 8. (Colour online) Phase-averaged PIV data for $A^* = 0.25$, $St = 0.32$ showing contour plots of vorticity ω. (*a*) $D^* \gg 1$; (*b*) $D^* = 0.5$. Foil is mid-upstroke ($\varphi = 0$).

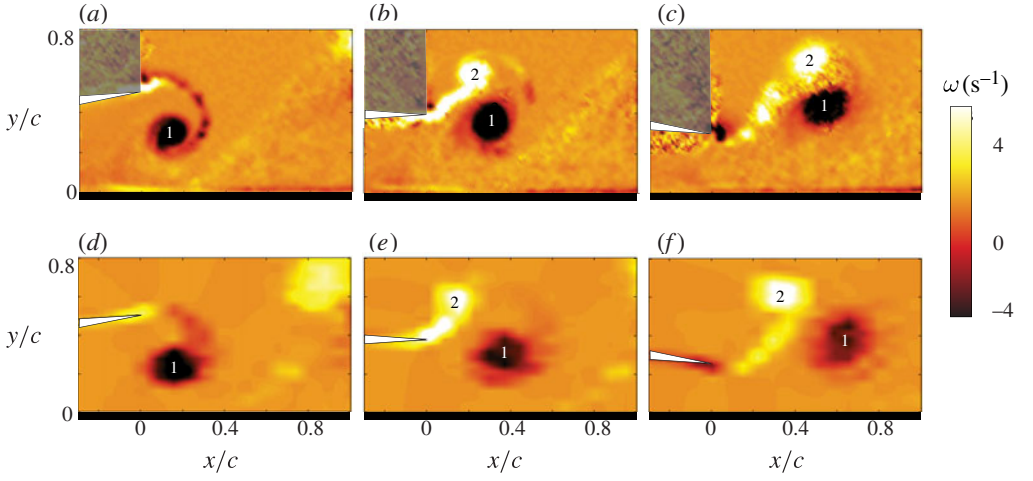

FIGURE 9. (Colour online) Vortex pairs at $D^* = 0.38$ for $A^* = 0.25$ and $St = 0.32$. (*a,b,c*) Phase-averaged PIV data; (*d,e,f*) potential flow computations. The phases shown are when the foil is at maximum θ, mid-downstroke, and minimum θ: (*a,d*) $\varphi = \pi/2$, (*b,e*) π, (*c,f*) $3\pi/2$.

The formation of vortex pairs is best explained using the method of images, where each vortex has an opposite-signed image vortex equidistant beneath the ground to satisfy the no-flux condition (see figure 4). Following the Biot-Savart law, the negative vortices will advect slower near the ground while the positive vortices will advect faster. The pairing process is shown in the data of figure 9 and illustrated using the method of images in figure 10(*a–c*). Vortex 1 is slowed by its opposite-signed image, so that it is still near the trailing edge of the foil when vortex 2 is shed. Then, driven by their mutual induction, vortices 1 and 2 move downstream and away from the ground before the cycle repeats (see figure 10). It is possible that the ground boundary layer also contributes to the slower advection of vortex 1 in the experiments, but since the behaviour of the vortex pairs is captured almost precisely by the inviscid computations, the slower advection appears to be primarily an inviscid phenomenon. Also shown in figure 9 is the distortion of the positive vortices. In both the PIV and computational data, the strongly negative vortex 1 enhances the shear layer in the wake of vortex 2, leaving a filament of positive vorticity trailing the vortex pair.

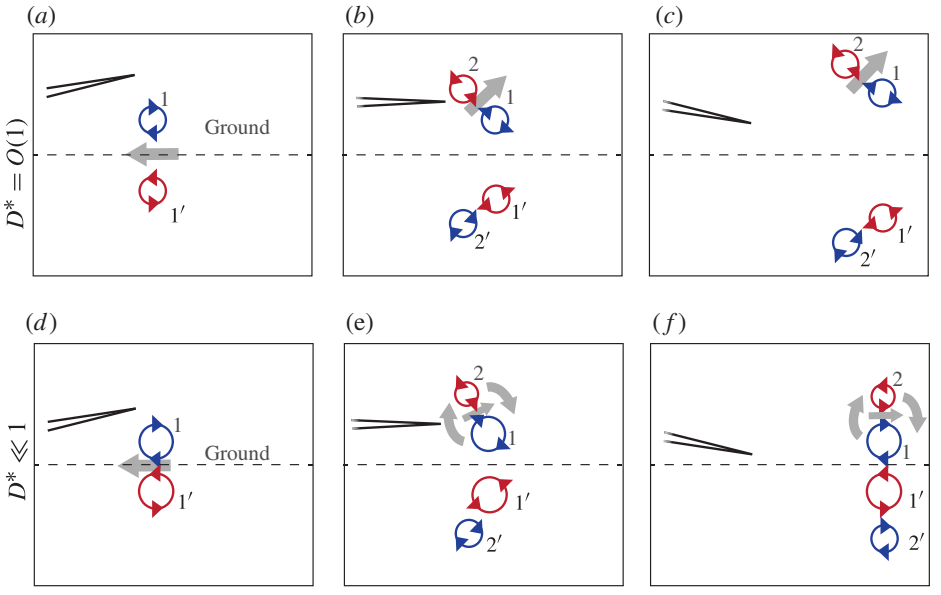

FIGURE 10. (Colour online) Wake dynamics explained with the method of images. (*a,b,c*) Moderate ground effect; (*d,e,f*) extreme ground effect. Image vortices are labelled with primes. Vortex strength is illustrated by its size. Grey arrows indicate regions of high velocity. (*a,d*) $\varphi = \pi/2$, (*b,e*) $\varphi = \pi$, (*c,f*) $\varphi = 3\pi/2$.

Vortices were found to form pairs for all near-ground conditions ($D^* < 1$), but in extreme ground effect ($D^* \leqslant 0.38$), they behaved slightly differently. Figure 11 shows vorticity contours for $D^* = 0.25$. In the experiment, vortex 1 was strong enough to detach the boundary layer along the ground and form the satellite vortex 3 underneath the trailing edge. Vortex 3 advects downstream in a wake that now contains three vortices per flapping cycle. As in the $D^* = 0.38$ case, a filament of positive vorticity trails the vortex pair, but in this case the filament rolls up into the positive satellite vortex 3. By comparing figures 9 and 11, we see that in moderate ground effect the vortices advect away from the ground, whereas in extreme ground effect they move approximately straight downstream. This discrepancy can be attributed to the strength of vortex 1, which becomes increasingly stronger than vortex 2 as the ground proximity decreases. This mismatch in magnitude causes vortex 2 to rotate in a clockwise sense about vortex 1, thus reorienting the pair such that it advects downstream (see figure 10).

The motion of the vortices leads to particular orientations for the time-averaged momentum field. When the wake vortices advect away from the ground, the time-averaged field displays a jet that angles upward, as seen in figure 12 for $D^* = 0.5$, where $\bar{u}$ is the time-averaged streamwise velocity and $\bar{U}^* = \bar{u}/u_\infty$. This behaviour is in contrast to the flow when the foil is far from the ground where the jet is directed straight downstream. When the foil is closer to the ground, the reoriented trajectory of the pair is such that the time-averaged jet angles back toward the ground, as seen in figure 12 for $D^* = 0.25$. Note also the regions of low mean velocity between the foil and the ground. This phenomenon is most pronounced at high Strouhal numbers and is caused by the upstream flow that is present beneath the foil during the upstroke.

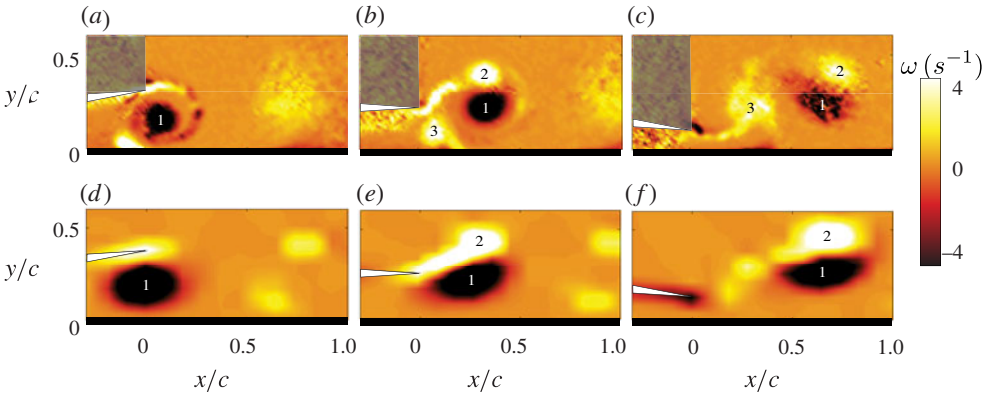

FIGURE 11. (Colour online) Vortex pairs at $D^* = 0.25$. (*a,b,c*) Phase-averaged PIV data. (*d,e,f*) potential flow computations. Conditions and phases as in figure 9: (*a,d*) $\varphi = \pi/2$; (*b,e*) $\varphi = \pi$; (*c,f*) $\varphi = 3\pi/2$.

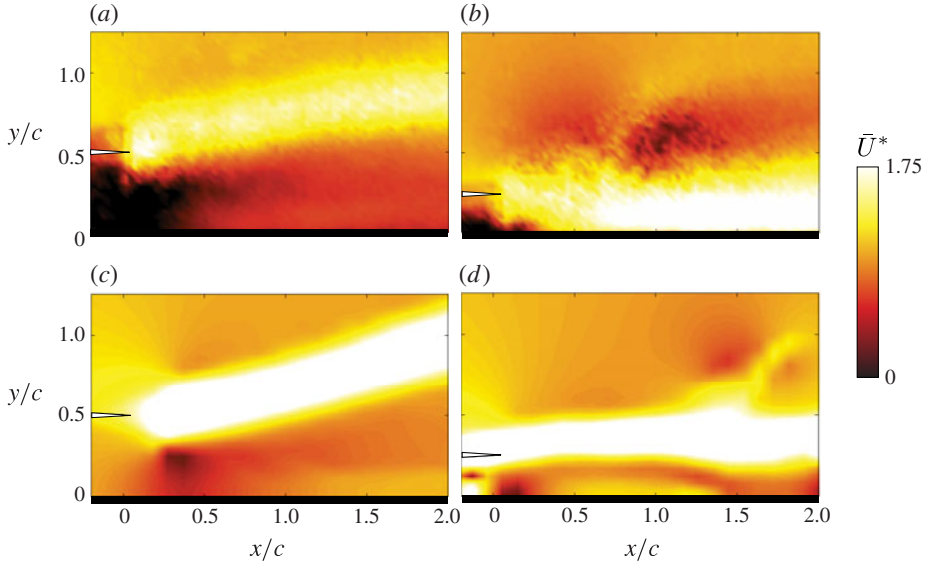

FIGURE 12. (Colour online) Time-averaged velocity fields for $A^* = 0.25$ and $St = 0.32$. (*a,c*) $D^* = 0.5$; (*b,d*) $D^* = 0.25$. (*a,b*) PIV data; (*c,d*) potential flow computations.

The time-averaged jets also offer insight into the origins of thrust production. Typical mean velocity profiles are shown in figure 13, including one taken in the absence of the foil, $\bar{u}_{BL}(y)$. Note the increase in magnitude of the peak velocity with increasing Strouhal number, and the regions of reduced velocity for $y/c < 0.5$. Such profiles can be used to calculate the net streamwise momentum flux p_x by integrating over a control surface. That is,

$$\bar{C}_{p_x} \equiv \frac{\bar{p}_x}{\frac{1}{2}\rho u_\infty^2 cs} = \int_0^{Y_2^*} \bar{U}^{*2}\,\mathrm{d}Y^* - \int_0^{Y_1^*} \bar{U}_{BL}^{*2}\,\mathrm{d}Y^* = \int_0^{Y_2^*} \bar{U}^*(\bar{U}^* - \bar{U}_{BL}^*)\,\mathrm{d}Y^*, \qquad (4.1)$$

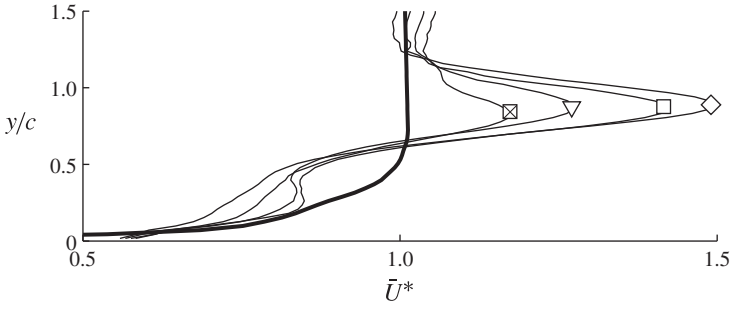

FIGURE 13. Time-averaged streamwise velocity profiles taken at a location $c/2$ downstream of the trailing edge. Sample data are shown are for $A^* = 0.25$ and $D^* = 0.875$, with $St = 0.19$ (⊠), $St = 0.22$ (▽), $St = 0.25$ (□), and $St = 0.28$ (◇). The bold line shows $\bar{U}^*_{BL}$, the non-dimensional time-averaged streamwise velocity when no foil is present.

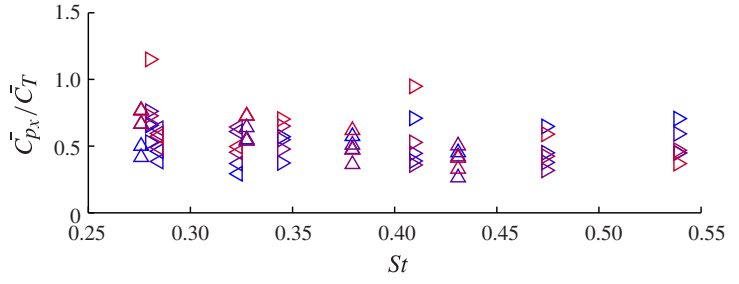

FIGURE 14. (Colour online) Streamwise momentum flux coefficient. $\bar{C}_{p_x}$ is plotted with the same scaling as suggested for the thrust coefficient. Symbols and notation as in figure 6.

using mass conservation. Here, $Y^* \equiv y/c$. This momentum flux differs from the thrust by about a factor of two, in that it neglects pressure differences over the control surface, and the shear stress applied by the ground. Nevertheless, figure 14 reveals that $\bar{C}_{p_x}/\bar{C}_T$ shows little dependence on St and D^*, suggesting that $\bar{C}_{p_x}$ follows a similar scaling as $\bar{C}_T$.

5. Lift production

The time-averaged angled jets impart momentum to the fluid in the cross-stream direction, suggesting that there is a net lift force produced by an unsteady aerofoil in ground effect even if its motion is symmetric. The lift force could not be measured in the experiment, but we can obtain some insight from the computations. The computations were run for 50 cycles since the lift converged more slowly than the thrust, power or efficiency. After 50 cycles, the lift changed by less than 5 % after doubling the number of cycles. Only one amplitude of motion, $A^* = 0.19$, is presented for clarity. The other amplitudes show similar trends. Two extra cases at $D^* = 0.29$ and 0.33 were added to show more continuous lift coefficient curves.

Figure 15 shows the time-averaged lift coefficient $\bar{C}_L$ as a function of D^* and St, where $\bar{C}_L = \bar{L}/(\rho u_\infty^2 cs/2)$, and $\bar{L}$ is the time-averaged lift averaged over the 50th cycle of motion. Two regimes in lift production may be distinguished. When $0.4 \lesssim D^* \lesssim 1$,

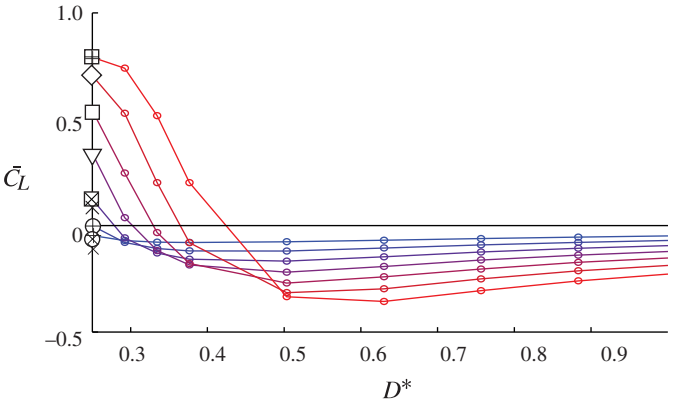

FIGURE 15. (Colour online) Time-averaged lift coefficient. ⊗, $St = 0.13$; ⊕, $St = 0.16$; ⊞, $St = 0.31$; other symbols as in figure 13.

the lift force is negative and tends to pull the aerofoil towards the ground, and when $0.25 \lesssim D^* \lesssim 0.4$, the lift force is positive and tends to push the aerofoil away from the ground. At $D^* \approx 0.4$ there is an equilibrium location where the time-averaged lift is zero. It is a stable equilibrium location in that any perturbation downward will cause a net positive lift and any perturbation upward will cause a net negative lift. It can also be seen that with increasing Strouhal number the equilibrium location moves further away from the ground, and within each regime the magnitude of the lift coefficient increases. At this equilibrium location where $D^* \approx 0.4$, the thrust enhancement is $\sim 40\,\%$.

6. Concluding remarks

In the range of ground proximities considered ($0.25 < D^* < 2.9$), the thrust capabilities of a pitching foil were shown to increase compared to its value far from the ground, while the propulsive efficiency remained independent of D^* within the uncertainty of the experiment. It appears that ground effects are advantageous for efficient thrust production using pitching foils, and could allow higher cruise speeds with no loss in efficiency. This result suggests that animals whose fins oscillate perpendicular to the ground, such as rays and skates, may experience benefits when swimming near the sea floor.

The effects of viscosity reduced the thrust and increased the required power at all Strouhal numbers tested, and the efficiency was reduced to about half its inviscid level for $St \geqslant 0.38$. Nevertheless, over most of the conditions considered, thrust and power were found to follow a power-law scaling described by $1 + D^{*-\beta}$, with $\beta = 0.4$ for both the inviscid computations and the experiments. The result is that thrust production increases monotonically as the foil approaches the boundary for $D^* \geqslant 0.25$. This finding was found to be almost independent of pitching amplitude and Strouhal number over the ranges $0.19 \leqslant A^* \leqslant 0.31$ and $0.25 \leqslant St \leqslant 0.45$.

The wake structures generated by near-ground pitching foils were found to be markedly different from those observed far from the ground. The vortices shed into the wake were found to form pairs behind the foil, and for $D^* > 0.38$ they were advected away from the ground and created angled jets of mean momentum. This finding offers a more general explanation for the wake vortex structure attributed to

foil camber by Molina & Zheng (2011). Additionally, filaments of positive vorticity were observed trailing the vortex pairs. When $D^* \leqslant 0.38$, vortex pairs curved back toward the ground, causing the momentum jet to point straight downstream.

Two regimes of lift production were identified in the computations. The first regime occurred at ground proximities of $0.4 \lesssim D^* \lesssim 1$ where negative lift was generated that pulled the aerofoil towards the ground. The second regime occurred at ground proximities of $0.25 \lesssim D^* \lesssim 0.4$ where positive lift was generated that pushed the aerofoil away from the ground. Between these two regimes a stable equilibrium location exists where the time-averaged lift was zero and a thrust enhancement of $\sim$40 % was measured. This stable equilibrium location may offer significant performance gains for animals swimming or flying near solid boundaries.

Acknowledgements

The authors would like to thank B. Boschitsch for helping design and construct the experimental apparatus used in this investigation. The authors would also like to thank Q. Zhou for helping obtain results for the numerical validation. This work was supported by the Office of Naval Research under Program Director Dr B. Brizzolara, MURI grant number N00014-08-1-0642.

Appendix A. Potential flow method validation

The free parameters for the numerical solution were the trailing-edge Kutta condition panel orientation and length, the desingularization radius for the wake elements, the collocation point location, the number of body elements N, and the number of wake elements per time step N_{step}.

A trailing-edge doublet element is used to enforce the Kutta condition of finite velocity at the trailing edge by having a strength that cancels the vorticity at the trailing edge. The orientation of the element was set to be along a line that bisects the angle of the trailing edge, which is typical for steady flow conditions (Katz & Plotkin 2001). Traditionally, the trailing-edge element length is set to 0.3–$0.5u_\infty \Delta t$ (Willis *et al.* 2007), where $\Delta t = 1/(f N_{step})$. Here a length of $0.4u_\infty \Delta t$ was used since it gave good solution convergence while maintaining solution accuracy for the validation cases. The desingularization radius was set to $\epsilon = 2.5 \times 10^{-5} c$. A Dirichlet boundary condition is applied where the velocity potential within the body is held constant, which indirectly enforces the no-flux boundary condition through the aerofoil surface. As such, the collocation points must be within the body. In our method, they were located at the centre of the elements but moved into the body by 15 % of the distance to the neutral axis of the aerofoil at that point, along the element normal vector.

Both the number of body elements and the number of time steps per cycle were varied and the time-averaged thrust coefficient, power coefficient and propulsive efficiency were tracked as shown in figure 16. The flapping parameters used for convergence studies were $c = 0.08$ m, $St = 0.3$, $A^* = 0.25$, $u_\infty = 0.06$ m s^{-1} with a 10 % thick teardrop aerofoil shape following Godoy-Diana *et al.* (2009). Eight flapping cycles were run and the time-averaged quantities were taken over the last flapping cycle. When the number of body panels was doubled from $N = 250$ to $N = 500$ (with $N_{step} = 200$) the coefficient of thrust and efficiency changed by less than 1 % while the power coefficient changed by less than 2 %. When the number of time steps was doubled from $N_{step} = 150$ to $N_{step} = 300$ (with $N = 200$), the coefficient of thrust and efficiency changed by less than 1 % while the power coefficient changed by less than 2 %. Therefore, for all calculations in this study, we used $N = 250$ and $N_{step} = 150$.

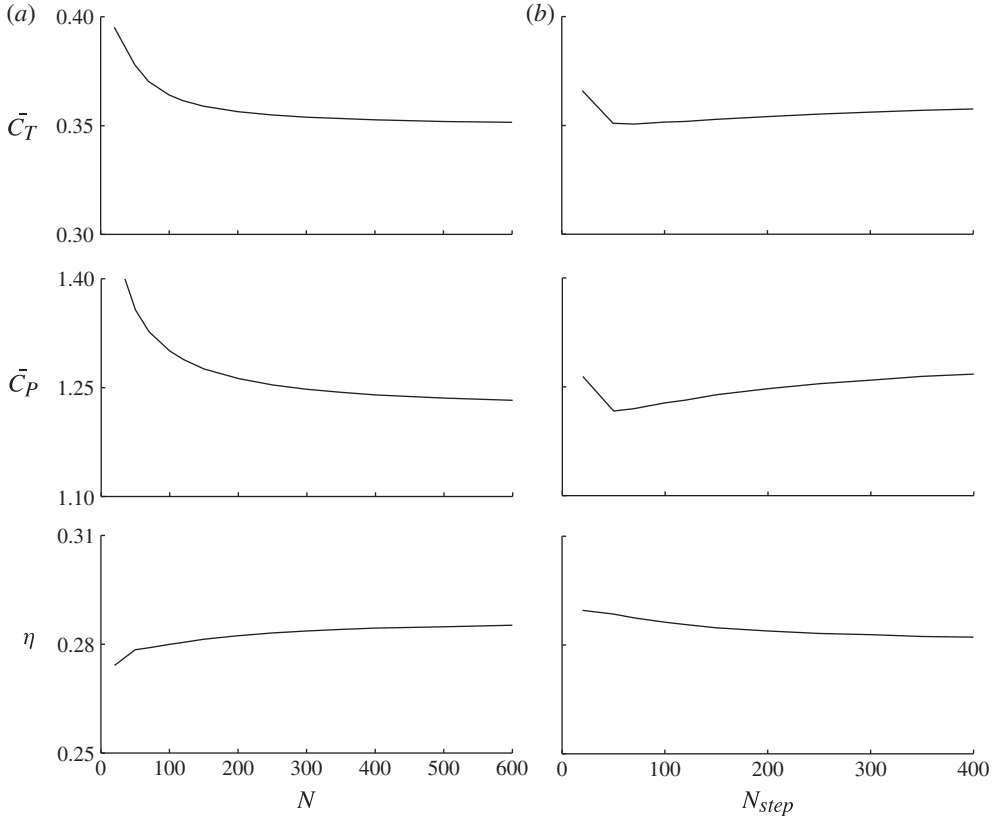

FIGURE 16. Convergence of the numerical solution with (*a*) increasing number of body panels N and (*b*) increasing number of time steps per cycle N_{step}.

To validate the accuracy of the boundary element method a series of exact analytical potential flow solutions were compared to the numerical calculations. First, the steady pressure distribution over a two-dimensional van de Vooren aerofoil was used, which has an analytical solution (van de Vooren & de Jong 1970) and it has a finite-angle trailing edge as in our experiment. Figure 17 shows excellent agreement between the analytical and numerical solutions. In these validation cases the time step was $\Delta t = 6.67$ s, $u_\infty = 5$ m s^{-1}, $c = 1$ m, with $N = 150$. The starting vortex from the time-stepping solution was allowed to advect downstream $1000c$ before the coefficient of pressure was calculated.

Second, the unsteady lift produced by a small-amplitude two-dimensional heaving plate from the Theodorsen (1935) model was compared to the numerical solution. The Theodorsen model for a pure heaving motion can be cast into a non-dimensional form,

$$C_L = -2\pi^2\, St|C(k)|\cos(2\pi\tau + \phi) - \pi^2 St\, k \sin(2\pi\tau) \qquad \text{(A 1)}$$

where $C_L = 2L/\rho c u_\infty^2$, $h = h_0 \sin(2\pi\tau)$, $St = 2h_0 f/u_\infty$, $k = \pi f\, c/u_\infty$, and $\tau = f\, t$.

Here, h is the time-varying heave, k is the reduced frequency, $|C(k)|$ is the magnitude and ϕ is the phase angle of the lift deficiency factor which is a complex number. A 0.1 % thick teardrop-shaped aerofoil was used to simulate an infinitesimally

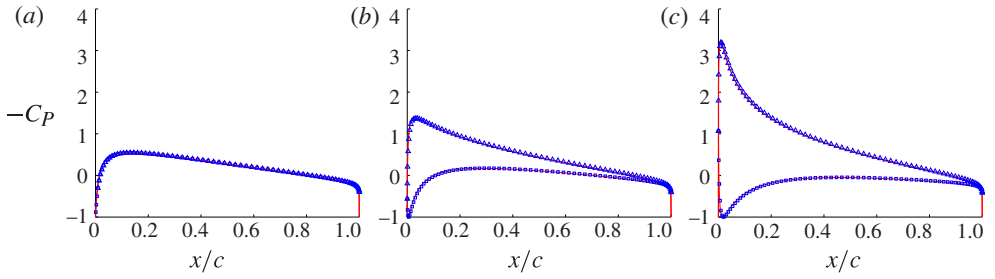

FIGURE 17. (Colour online) Coefficient of pressure over the top and bottom surfaces of a 15 % thick van de Vooren aerofoil. (*a*) $\alpha = 0$, (*b*) 4°, and (*c*) 8°. ———, Analytical solution; △, numerical solution for the top surface; □, numerical solution for the bottom surface.

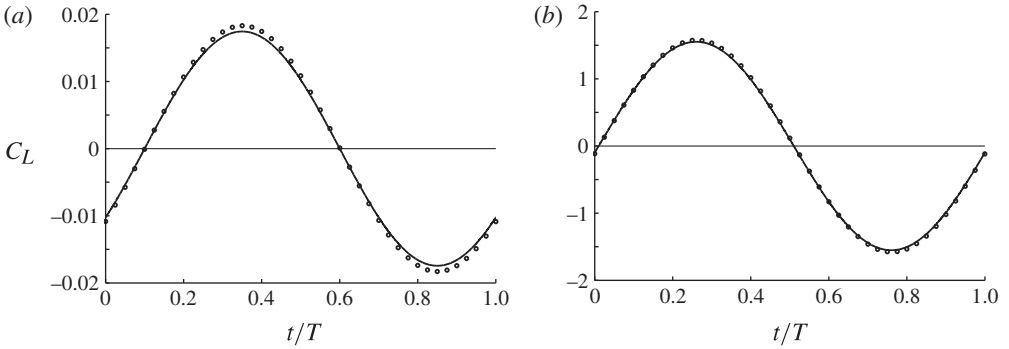

FIGURE 18. Lift coefficients during one pitching period T, for $c = 1$, $u_\infty = 1$, $h/c = 0.01$, $N = 350$, $N_{step} = 250$. (*a*) $St = 0.001$, $k = 1.57$. (*b*) $St = 0.01$, $k = 15.7$. ———, Theodorsen model; ○, numerical solution.

thin plate. The force measurements were taken from the eighth flapping cycle. A frozen wake, which did not advect with the local velocity, was used to simulate the assumptions in the Theodorsen model. As can be seen from figure 18, there was excellent agreement between the analytical and numerical solutions.

Appendix B. Thrust and power scaling for $A^* \ll 1$

The lowest reduced frequency considered here is approximately 4.2. Typical lateral velocities are therefore much higher than typical streamwise velocities, and we will focus on non-circulatory lift forces (added mass forces) when scaling the lift or lateral force L on the foil. Accordingly, we introduce a representative added mass $m^* = \rho c^2 s$. The accelerations of this added mass come from two sources. The first is due to the lateral acceleration of the foil which is proportional to $c\ddot{\theta}$, and the second is due to the time-varying circulation around the foil. From thin aerofoil theory, we expect the velocity above and below the foil to scale with $u_\infty(1 \mp \theta)$, and so the streamwise accelerations will scale with $u_\infty\dot{\theta}$. Because these are small-amplitude arguments, the lift due to added mass is expected to vary with a linear combination of these two contributions, that is,

$$L \sim m^*(C_1 c\ddot{\theta} + C_2 u_\infty \dot{\theta}), \tag{B 1}$$

where C_1 and C_2 are constants. These are precisely the non-circulatory lift terms in the Theodorsen (1935) model, here introduced via a scaling argument. Theodorsen determined that $C_1 = \pi/4$ and $C_2 = \pi/8$.

The lateral force is of interest because it relates to the thrust and the power input to the fluid. As originally noted by Knoller (1909) and Betz (1912), the thrust of an oscillating foil is directly proportional to the lift: it is merely the component of lift in the streamwise direction, that is, $T = L\sin(\theta) \approx L\theta$ for small angles. The moment on the foil scales with Lc and so the power input scales with $Lc\dot{\theta}$. The motions considered here are purely sinusoidal, so that $\dot{\theta}$ is orthogonal to θ and $\ddot{\theta}$. This causes the expressions for thrust and power to simplify greatly when time-averaged over one flapping cycle, and we find

$$\bar{T} \sim \int_{t_0}^{t_0+1/f} L\theta \,\mathrm{d}t \sim m^* c \int_{t_0}^{t_0+1/f} \ddot{\theta}\theta \,\mathrm{d}t, \tag{B 2}$$

$$\bar{P} \sim \int_{t_0}^{t_0+1/f} Lc\dot{\theta} \,\mathrm{d}t \sim m^* c u_\infty \int_{t_0}^{t_0+1/f} \dot{\theta}^2 \,\mathrm{d}t. \tag{B 3}$$

By introducing $\Theta \equiv \theta/A^*$ and $\tau = f\,t$, this can be written in dimensionless form as

$$\bar{C_T} \sim St^2 \int_{\tau_0}^{\tau_0+1} \ddot{\Theta}\Theta \,\mathrm{d}\tau \quad \text{and} \quad \bar{C_P} \sim St^2 \int_{\tau_0}^{\tau_0+1} \dot{\Theta}^2 \,\mathrm{d}\tau, \tag{B 4}$$

so that that $\bar{C_T}$ and $\bar{C_P}$ are expected to scale with St^2 for small-amplitude flapping. The scaling for C_T is consistent with Dewey *et al.* (2013), who used a similar added mass argument to arrive at the first term in our expression for L. By introducing both terms, we have accounted for orthogonality in our model and arrived at a different scaling for C_P.

REFERENCES

BAUDINETTE, R. V. & SCHMIDT-NIELSEN, K. 1974 Energy cost of gliding flight in herring gulls. *Nature* **248**, 83–84.

BETZ, A. 1912 Ein beitrag zur erklaerung des segelfluges. *Z. Flugtech. Motorluftschiff.* **3**, 269–270.

BLAKE, R. W. 1979 The energetics of hovering in the mandarin fish (Synchropus picturatus). *J. Expl Biol.* **82**, 25–33.

BLEVINS, E. & LAUDER, G. V. 2012 Rajiform locomotion: three-dimensional kinematics of the pectoral fin surface during swimming by freshwater stingrey Potamotrygon orbignyi. *J. Expl Biol.* **215**, 3231–3241.

BLEVINS, E. & LAUDER, G. V. 2013 Swimming near the substrate: a simple robotic model of stingrey locomotion. *Bioinspir. Biomim.* **8**, 016005.

BUCHHOLZ, J. H. J. & SMITS, A. J. 2008 The wake structure and thrust performance of a rigid low-aspect-ratio pitching panel. *J. Fluid Mech.* **603**, 331–365.

COULLIETTE, C. & PLOTKIN, A. 1996 Airfoil ground effect revisited. *Aeronautical Journal* **100** (992), 65–74.

DEWEY, P. A., BOSCHITCH, B. M., MOORED, K. W., STONE, H. A. & SMITS, A. J. 2013 Scaling laws for the thrust production of flexible pitching panels. *J. Fluid Mech.* **732**, 29–46.

DRUCKER, E. G. & LAUDER, G. V. 2001 Locomotor function of the dorsal fin in teleost fishes: experimental analysis of wake forces in sunfish. *J. Expl Biol.* **204**, 2943–2958.

GODOY-DIANA, R., MARAIS, C., AIDER, J. & WESFREID, J. E. 2009 A model for the symmetry breaking of the reverse Bénard–von Kármán vortex street produced by a flapping foil. *J. Fluid Mech.* **622**, 23–32.

HAINSWORTH, F. R. 1988 Induced drag savings from ground effect and formation flight in brown pelicans. *J. Expl Biol.* **135**, 431–434.

IOSILEVSKII, G. 2008 Asymptotic theory of an oscillating wing section in weak ground effect. *Eur. J. Mech.* **27**, 477–490.

KANG, C. K., AONO, H., BAIK, Y. S., BERNAL, L. P. & SHYY, W. 2013 Fluid dynamics of pitching and plunging flat plate at intermediate Reynolds numbers. *AIAA J.* **51** (2), 315–329.

KATZ, J. & PLOTKIN, A. 2001 *Low-Speed Aerodynamics*. 13th edn. Cambridge University Press.

KNOLLER, R. 1909 Die gesetze des luftwiderstandes. *Flug- Motortech.* **3** (21), 1–7.

KRASNY, R. 1986 Desingularization of periodic vortex sheet roll-up. *J. Comput. Phys.* **65** (2), 292–313.

LIU, P., WANG, T., HUANG, G., VEITCH, B. & MILLAN, J. 2010 Propulsion characteristics of wing-in-ground effect dual-foil propulsors. *Appl. Ocean Res.* **32**, 103–112.

MOLINA, J. & ZHENG, X. 2011 Aerodynamics of a heaving aerofoil in ground effect. *AIAA J.* **49**, 1168–1179.

MORYOSSEF, Y. & LEVY, Y. 2004 Effect of oscillations on aerofoils in close proximity to the ground. *AIAA J.* **42**, 1755–1764.

PAN, Y., DONG, X., ZHU, Q. & YUE, D. K. 2012 Boundary-element method for the prediction of performance of flapping foils with leading-edge separation. *J. Fluid Mech.* **698**, 446–467.

PARK, H. & CHOI, H. 2010 Aerodynamic characteristics of flying fish in gliding flight. *J. Expl Biol.* **213**, 3269–3279.

ROZHDESTVENSKY, K. V. 2006 Wing-in-ground effect vehicles. *Prog. Aerosp. Sci.* **42**, 211–283.

SCHNIPPER, T., ANDERSEN, A. & BOHR, T. 2009 Vortex wakes of a flapping foil. *J. Fluid Mech.* **633**, 411–423.

SCIACCHITANO, A., WIENEKE, B. & SCARANO, F. 2013 PIV uncertainty quantification by image matching. *Meas. Sci. Technol.* **24** (045302).

STANISLAS, M., OKAMOTO, K., KAHLER, C. J. & WESTERWEEL, J. 2005 Main results of the second international PIV challenge. *Exp. Fluids* **39**, 170–191.

TANIDA, Y. 2001 Ground effect in flight. *JSME* **44**, 481–486.

THEODORSEN, T. 1935 General theory of aerodynamic instability and the mechanism of flutter. *Tech. Rep.* National Advisory Committee for Aeronautics.

VAN DE VOOREN, A. I. & DE JONG, L. S. 1970 Calculation of incompressible flow about aerofoils using source, vortex or doublet distributions. *Tech. Rep.* Math. Inst. of the University of Groningen, The Netherlands.

WEBB, P. W. 1993 The effect of solid and porous channel walls on steady swimming of stealhead trout, Oncorhynchus mykiss. *J. Expl Biol.* **178**, 97–108.

WIE, S. Y., LEE, S. & LEE, D. J. 2009 Potential panel and time-marching free-wake coupling analysis for helicopter rotor. *J. Aircraft* **46** (3), 1030–1041.

WILLIS, D. J., PERAIRE, J. & WHITE, J. K. 2007 A combined PFFT-multipole tree code, unsteady panel method with vortex particle wakes. *Intl J. Numer. Meth. Fluids* **53** (8), 1399–1422.

WITHERS, P. C. & TIMKO, P. L. 1977 The significance of ground effect to the aerodynamic cost of flight and energetics of the black skimmer (Rhyncops nigra). *J. Expl Biol.* **70**, 13–26.

ZHU, Q. 2007 Numerical simulation of a flapping foil with chordwise or spanwise flexibility. *AIAA J.* **45** (10), 2448–2457.